Numerical Simulation of Steady and Pulsating Flow over an Isothermal Cylinder with Varying Corner Radius

Ahmed G. Rahma[1], and Talaat Abdelhamid[2]*

***Abstract*— This paper presents a numerical simulation of the flow structure, flow topology, and heat transfer of an isothermal cylinder with variable corner radius ratio (*r/R*) = 0, 0.1, 0.25, 0.5, 0.75, and 1.0, for two different flow regimes. One is steady and the other is pulsating flow. Here, *r* is the corner radius and *R* is the cylinder half-width. The air stream flow has a low Reynolds number *Re* of 100 and Prandtl number *Pr* = 0.7. The dimensionless amplitude of the velocity oscillations (A^*) is 40% relative to the free-stream velocity, and the dimensionless frequency is 7. The governing equations were solved using the ANSYS-FLUENT 19.2 package. The Pressure implicit with the splitting of the operator algorithm PISO is used for the pressure-velocity coupling. The results from the models agree with those in the literature. The effect of *r/R* on the flow structure around the cylinder is investigated for steady and pulsating flow regimes. Increasing *r/R* leads to the appearance of two major flow patterns around the cylinder. Pattern A appears at *r/R* < 0.1, which has leading-corner separation and two secondary bubbles appear on the sides of the cylinder. Pattern B appears at *r/R* > 0.1, which has trailing-corner separation. The time-mean drag coefficient ($\bar{C}_D$) for the pulsating flow is higher than that of the steady flow overall *r/R*. For the pulsating flow, $\bar{C}_D$ increases by about 5.37% overall *r/R*. The surface- and time-averaged Nusselt number increases with increasing *r/R* for both flow regimes.**

***Keywords*— Flow structure, heat transfer, vortex shedding, steady and pulsating flow, wake structure, CFD.**

I. INTRODUCTION

The convection heat transfer and fluid flow over cylinders with various shapes have garnered significant attention in applications such as heating, ventilation, air conditioning, heat exchangers, and the enhancement of cooling systems for electronic chips [1]–[3]. Saha et al. [4] conducted a numerical investigation to explore the spatial evolution of vortices and the transition to three-dimensionality in the wake of a square cylinder. They found that the transition to three-dimensionality occurs at a Reynolds number (*Re*) between 150 and 175. Two types of secondary vorticity modes were observed: Mode-A appeared at *Re* = 175 - 240, and Mode-B appeared at *Re* ≥ 250, characterized by predominantly small-scale structures. At *Re* = 250, the transition from Mode-A to Mode-B was defined by a simultaneous discontinuity in the frequency law. The results also indicated that the time-averaged drag coefficient values for the square cylinder were closely related to the Reynolds number spectrum of interest and reflected the spatial structure. Abdelhamid et al. [5] conducted a study on the flow structure and heat transfer around an isothermal cylinder with a corner radius ratio (*r/R*) of 0.5, at variable angle of attack (α) ranging from 0° to 45°, and *Re* of 180. Here, *r* represents the corner radius, and *R* is the half-side width of the cylinder normal to the freestream direction. Two major flow regimes were observed: Flow regime A appeared at α = 0° - 8.5° and was defined as trailing corner separation flow, while flow regime B appeared in the range of α > 8.5° - 45° and was defined as leading-trailing separated flow. The flow structure was found to be unsteady and characterized by alternating Kármán vortices. Zafar and Alam, [6] investigated the effect of *r/R* on the heat transfer over the cylinder surface. The simulations were performed at *Re* = 150 and Prandtl number (*Pr*) of 0.7. The modification of *r/R* from 0.0 to 1.0 led to an approximate 33% enhancement in heat transfer. Additionally, this modification resulted in the shrinkage of the wake bubble and an increase in the vortex of shading length. Gau, et al. [7] conducted an experimental study to investigate the heat transfer and vortex flow of an oscillating isothermal cylinder in the crossflow direction with varying frequencies. The results revealed a simultaneous enhancement in heat transfer at the stagnation point in the downstream region. The study of time-averaged and fluctuating forces is of significant importance, as the convection heat transfer and aerodynamic characteristics mutually influence each other [4]. Badr, [8] conducted a numerical analysis to study the effect of freestream fluctuations on laminar convection over an isothermal cylinder. The simulations were conducted at average *Re* from 50 to 500, with the amplitude of velocity oscillations *A** ranging from 20% to 50% of the freestream average velocity. The findings revealed that the rate of heat transfer increases with the increase of the amplitude but decreases with the increase of frequency. Singh and Engg [9] performed a numerical study to investigate the effect of the *r/R* on heat

Manuscript received [04 November 2023]; accepted [05 November 2023]. Date of publication [17 January 2024].

This work was partially supported by the Science and Technology Development Fund (STDF) of Egypt, project No: 39385. (*Corresponding author: Talaat Abdulhamid)

[1]Ahmed G. Rahma is with Department of Physics and Engineering, University of Strasbourg, 4 Rue Blaise Pascal, 67081 Strasbourg, France, (email: ahmedgrahma@outlook.com).

[2]Talaat Abdulhamid is with Faculty of Electronic Engineering, Department of Physics and Engineering Mathematics, , Menouf 32952, Menoufia University ,Egypt (email: talaat_abdelhamid@el-eng.menofia.edu.eg).

transfer and flow structure over two different cylinders, one with sharp edges and the other with rounded edges. The simulations were performed at Re = 100 and Pr = 0.7. The results showed that using rounded edges resulted in smoother flow separation compared to the square cylinder, and delayed flow instability. The drag coefficient decreased due to a reduction in pressure drag. Furthermore, the heat transfer from the cylinder was significantly enhanced due to the corner modification, with an average enhancement of 17% for the cylinder with rounded edges. Ambreen and Kim [10] conducted a study on the flow and heat transfer characteristics around a square cylinder with edge modifications. The simulations were performed at Re ranging from 55 to 200, with corner variations from corner size to cylinder width of 0.125. The mean surface Nusselt number was found to increase with increasing Re but decrease with the corner modification.

Changing the geometry and the flow regime are factors that are utilized to enhance heat transfer properties, resulting in higher heat transfer efficiency [11]–[13]. Gaheen, O. A. et al. [14] conducted an experimental study to investigate convection heat transfer enhancement from a circular cylinder in laminar pulsating flow with pulsating frequency from 1Hz to 12 Hz and Re from 1.02 10^4 to 2.04 10^4. Abdelhamid et al., [15] introduced a numerical simulation for an isothermal curved cylinder with a corner radius ratio r/R (= 0.5), attack angle (α) varies between $0° \leq \alpha \leq 45°$ at low Reynolds number Re (= 180). They observed that the fluid forces such as $\bar{C}_D$ and $\bar{C}_L$ are sensitive and have critical values at $\alpha \approx 5°$ and $\alpha \approx 12°$, respectively. They found that increasing α from 0° to 45° leads to a 12.9 % improvement in the heat transfer. Gupta et al. [16] conducted a numerical analysis to investigate the momentum and heat transfer characteristics of pulsating flow over a circular cylinder at various Re ($0.1 \leq Re \leq 40$), Pr ($0.7 \leq Pr \leq 100$), power-law indices ($00.3 \leq n \leq 1.4$), frequencies from 0 to π, and amplitudes from 0 to 0.8. The results showed that heat transfer could be improved by utilizing pulsating flow at appropriate Reynolds numbers, velocity amplitudes, and power-law indices.

The pulsating flow has a significant impact on vortex shedding and aerodynamic properties, leading to enhanced heat transfer. Khalid et al. [17] investigated the effect of pulsating flow over a square cylinder at Re of 100 with variable A^* of 0.2, 0.4, and 0.6. The results showed that the time-mean drag and fluctuating lift coefficients, as well as the averaged Nusselt number, increased with increasing A^*, regardless of the Richardson number (Ri). Yu et al. [18] performed two-dimensional numerical simulations to investigate the impact of pulsating flow on flow structure and heat transfer around a heated square cylinder at Re of 100, with varying A^* from 0.2 to 0.8, and normalized frequency (f^*) from 0 to 20. The results showed that the drag force increased with increasing amplitude at the same frequency and increased with increasing f^* from 0 to 5, followed by a decrease in the range of 5 to 20. Saxena and Ng, [19] investigated the impact of laminar pulsating flow on a heated rectangular cylinder at Re of 100, Pr of 0.74, variable aspect ratio ranging from 1 to 8, frequency of 4, and amplitude ratio of 0.4. The findings revealed that the heat transfer from the cylinder decreased with increasing aspect ratio. Additionally, natural vortex shedding occurred for lower aspect ratio cylinders.

The primary concept behind employing fluid flow in various applications is to manage heat and fluid dynamics around cylindrical structures, such as air conditioning systems, heat exchangers, electronic components on motherboards, and even in nuclear power plant operations involving flow over fuel rods.

The aim of this paper is to conduct a numerical investigation for the flow structure and heat transfer over a cylinder with variable r/R (= 0 – 1), A^* (= 0 – 0.8), and f^* = 0 – 21, at Re = 100 and Pr = 0.7 (air). The remainder of this paper is organized as follows: In section 2, we presented the problem description and the system of incompressible Navier-Stokes equations with a fully implicit finite element discretization. Furthermore, validation with literature review is introduced for the steady flow ($A^* = 0$) and pulsating flow ($A^* = 0.4$). In section 3, the CFD simulations are conducted to investigate the dependence of $\bar{C}_D$ and $\langle \overline{Nu} \rangle$ on the flow topology, wake structure, and heat transfer. Some concluding remarks are given in Section 4. The novelty in this research lies in the introduction of pulsating flow over the cylinder, which is uncommon in industrial applications. This novel approach demonstrates substantial improvements in heat and fluid properties. In this study, we aim to establish a new protocol for determining crucial parameters like pulse frequency and amplitude, which can have a significant impact on the overall performance.

II. NUMERICAL METHODOLOGY

A. Governing equations and physical model:

The governing continuity, energy, and momentum equations introduce in a laminar viscous and two-dimensional incompressible flow in the dimensionless form with constant properties over a cylinder with variable curved corners as follows:

The continuity equation,

$$\frac{\partial u^*}{\partial x^*} + \frac{\partial v^*}{\partial y^*} = 0, \quad (1)$$

The energy equation,

$$\frac{\partial \Theta^*}{\partial t^*} + u^* \frac{\partial \Theta^*}{\partial x^*} + v^* \frac{\partial \Theta^*}{\partial y^*} = \frac{1}{Re\, Pr}\left(\frac{\partial^2 \Theta^*}{\partial x^{*2}} + \frac{\partial^2 \Theta^*}{\partial y^{*2}}\right). \quad (2)$$

The momentum equations,

$$\frac{\partial u^*}{\partial t^*} + u^* \frac{\partial u^*}{\partial x^*} + v^* \frac{\partial u^*}{\partial y^*} = -\frac{\partial p^*}{\partial x^*} + \frac{1}{Re}\left(\frac{\partial^2 u^*}{\partial x^{*2}} + \frac{\partial^2 u^*}{\partial y^{*2}}\right), \quad (3)$$

$$\frac{\partial v^*}{\partial t^*} + u^* \frac{\partial v^*}{\partial x^*} + v^* \frac{\partial v^*}{\partial y^*} = -\frac{\partial p^*}{\partial y^*} + \frac{1}{Re}\left(\frac{\partial^2 v^*}{\partial x^{*2}} + \frac{\partial^2 v^*}{\partial y^{*2}}\right), \quad (4)$$

Based on the freestream velocity U_∞, freestream temperature T_∞, and projection width (side width) $D = 2R$, (Fig. 1a). The parameters are rendered dimensionless as stream velocity $u^* = u/U_\infty$ cross-stream velocity $v^* = v/U_\infty$ and pressure $p^* = p/\rho U_\infty^2$, $x^* = x/D$, and $y^* = y/D$, time $t^* = t\, U_\infty/D$ and temperature $\Theta^* = (T - T_\infty)/(T_w - T_\infty)$, where T_W is the cylinder surface temperature, Reynolds number $Re = \rho\, U_\infty D/\mu$ and $Pr = \frac{c_p \mu}{k}$, with ρ, μ, c_p and k are the fluid density, dynamic viscosity, specific heat, and thermal conductivity, respectively. The cylinder has variable r/R = 0,

0.1, 0.25, 0.5, 0.75, and 1.0, exposed to two different inlet flow regimes. Where the bluff body shape leads to flow instability and airflow separation, which in turn increases both drag and heat transfer. The pulsating flow regime refers to the flow with dimensionless frequency $f^* = (f/f_n)$, where f is the variable vortex shedding frequency and f_n is defined by the vortex-shedding frequency of the steady flow at $A^* = 0$. Here, the normalized frequency $f^* = 0$, 3.5, 7, 14, and 21. The ratio between the amplitude of the velocity oscillations and the average free-stream velocity $A^* = 0$, 0.2, 0.4, and 0.6, while the steady flow regime refers to the flow at $A^* = 0$. Both regimes are expressed in the schematic of the computational domain and are shown in (Fig. 1b). Typical grid structures around the cylinder and zoomed-in view of grids around the cylinder are provided in Fig. 1*d*,*c*. The domain of the inlet and outlet boundaries is shown in Table 1.

TABLE I The domain dimension of the inlet and outlet boundaries

Flow location	Symbols	Value
Upstream	L_u	11.5D
Downstream	L_d	38.5D
Distance between the two lateral boundaries	H	20.0D

Where the cylinder exposed face diameter to the upstream $D/H = 5\%$, this ratio is called a blockage ratio [5,19 – 21].

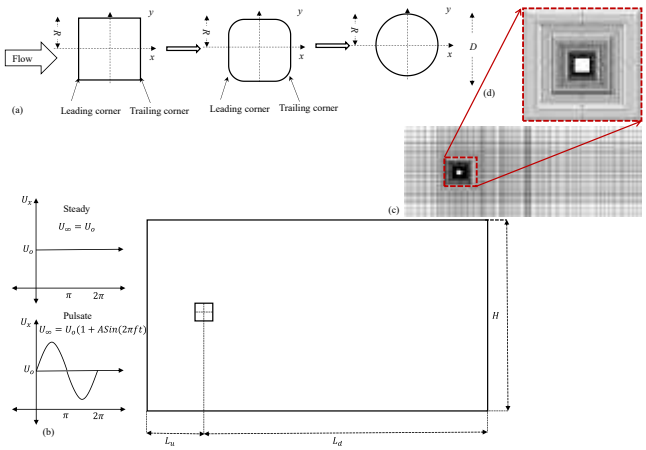

Fig. 1. *Computational domain parameters of two-dimensional cylinder with side length D = 2R. (a) cylinder with changing corner radius ratio, (b) Schematic of the computational domain, (c) Typical grid structure in the computational domain, (d) Zoomed-in view of grids around the cylinder.*

B. Boundary conditions, computational details, and flow parameters:

The boundary conditions are:

At the inlet for the constant flow,

$$u^*_{\text{Steady}} = 1,\ v^* = 0, \text{ and } \Theta^* = 0, \quad (5)$$

At the inlet for the pulsating flow

$$u^*_{\text{Pulsating}} = (1 + A\sin(2\pi ft)),\ v^* = 0, \text{ and } \Theta^* = 0 \quad (6)$$

At the outlet, $\frac{\partial \varphi^*}{\partial x^*} = 0$, where $\varphi^* = u^*, v^*$ and Θ^*, (7)

Slip conditions are not held on the surface of the cylinder,

$$u^* = 0 \text{ and } v^* = 0. \quad (8)$$

At conditions for the upper and lower boundaries,

$$\frac{\partial u^*}{\partial y^*} = 0,\ v^* = 0, \text{ and } \frac{\partial \theta^*}{\partial y^*} = 0. \quad (9)$$

The cylinder is considered as isothermal, i.e., $\Theta^* = 1$،

The drag and lift coefficients C_D and C_L are calculated as $C_D = 2F_D/\rho U_\infty^2 D$ and $C_L = 2F_L/\rho U_\infty^2 D$, where the drag and lift forces F_D and F_L are computed by integrating the pressure distribution and viscous shear force. The flow periodicity is defined by the frequency of vortex shedding. The local heat transfer coefficient h_θ over a cylinder surface at various positions θ *is* calculated from:

$$-k\frac{\partial T}{\partial n}|_w = h_\theta (T_w - T_\infty), \quad (10)$$

where n refers to the normal distance to the cylinder surface. The local Nusselt number is obtained as $Nu_\theta = h_\theta D/k$, time-averaged Nusselt number is obtained as $\overline{Nu} = \frac{1}{\tau}\int_0^\tau Nu_\theta\, dt$, surface-averaged Nusselt number is obtained as $\langle Nu \rangle = \frac{1}{s}\int_0^s Nu_\theta\, ds$, surface- and time-averaged Nusselt number is obtained as $\langle \overline{Nu} \rangle = \frac{1}{\tau}\int_0^\tau \langle Nu \rangle dt$, where s is the surface area of the cylinder, and τ is the integration time duration that varies from 60 to 80 vortex shedding cycles after the computation is converged.

The governing Navier–Stokes and energy equations (1 - 4) with the boundary conditions (5 - 10) are solved using the finite volume method with structured meshes. The numerical simulations are done using a commercial code ANSYS-FLUENT package. The PISO algorithm is used for the pressure-velocity coupling. The convective terms in the momentum and energy equations are discretized using the second-order upwind method. The temporal discretization for the transient solution is performed by the second-order backward Euler scheme. The convergence criteria for the continuity, x- and y-momentum, and energy equations is restricted beneath 10^{-6}. The flow is initialized with $u^* = 1$, $v^* = 0$, and $\Theta^* = 0$.

C. Mesh and validation:

Around the cylinder, an O-xy grid system and rectangular grid system are obtained as in Fig. 1d, where 320 points are evenly distributed around the cylinder and 120 points are distributed radially perpendicular to the cylinder surface. The first grid was 0.001D with 1.03 growing rate in the radial direction in relation to the cylinder surface. Table 2 introduces a comparison of the present results of $\bar{C}_D$ and $\langle \overline{Nu} \rangle$ with those obtained from the literature at the steady flow for $Re = 100$ and $r/R = 0$. The maximum variation of $\bar{C}_D$ is about 2.94% appears in the comparison with Sohankar et al, [21]. The surface- and time-averaged Nusselt number $\langle \overline{Nu} \rangle$ has a good agreement with that obtained from Alam et al, [23]. Table 3 presents a comparison of $\bar{C}_D$ and $\langle \overline{Nu} \rangle$ with those obtained from the literatures for the pulsating flow at $A^* = 0.4$ and $f^* = 7$. The obtained results have an agreement with the literature.

TABLE II Comparison of the obtained results with the literature at steady flow, $Re = 100$, $r/R = 0$

Reference	$\bar{C}_D$	(Error %)	$\langle \overline{Nu} \rangle$	(Error %)
Alam et al, 2020 [23]	1.50845	(0.240 %)	4.0	(0.377%)

Sohankar et al, 1998 [21]	1.46186	(2.939 %)	-	
Ambreen et al, 2018 [10]	1.4735	(2.126 %)	-	
Sharma et al, 2010 [24]	1.49292	(0.798 %)	-	
Present	1.50483		3.98	

TABLE III Comparison of the obtained results with the literature at $A^* = 0.4$, $Re = 100$, and $r/R = 0$.

Reference	$\bar{C}_D$	(Error %)	$\langle \overline{Nu} \rangle$	(Error %)
Khalid, et al, [17]	1.60	(0.62 %)	4.31	(5.3 %)
Jiu-Yang Yu et al, [18]	1.54	(4.54%)	4.26	(4.22 %)
Present	1.61		4.08	

III. Result and Discussions:

A. Time-mean drag force and Nusselt number:

Fig. 2(a) presents the effect of $\bar{C}_D$ on the dimensionless frequency f^*. The time mean drag coefficient $\bar{C}_D$ increases with increasing f^* from 0 up to 7 and then sharply decreases. Fig. 2(b) shows the variation of $\langle \overline{Nu} \rangle$ on the frequency f^* (= 0 – 21). The surface- and time-averaged Nusselt number $\langle \overline{Nu} \rangle$ slightly increases with increasing f^* from $f^* = 0$ up to 10, after that sharply decreases with increasing f^* from 12 to 21. The time mean drag coefficient $\bar{C}_D$ and $\langle \overline{Nu} \rangle$ correspond with increasing f^*. It is observed that $f^* = 7$, gives appropriate $\bar{C}_D$ and $\langle \overline{Nu} \rangle$. Hence, it is observed that $\bar{C}_D$ and $\langle \overline{Nu} \rangle$ have similar behavior with increasing f^* at $r/R = 0$.

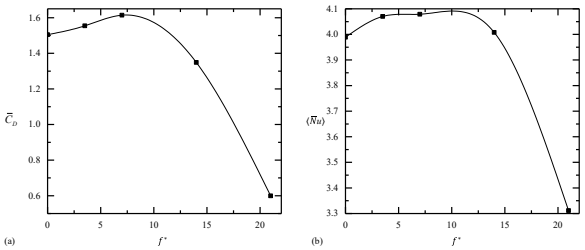

Fig. 2. *Effect of (a) time-mean drag coefficient $\bar{C}_D$ on the normalized frequency f^* and (b) surface- and time-averaged Nusselt number $\langle \overline{Nu} \rangle$ at $r/R = 0$ and $A^* = 0.4$, $Re = 100$, and $f^* = 0 – 21$.*

Figure 3 shows the effect of $\bar{C}_D$ and $\langle \overline{Nu} \rangle$ on A^* from 0 to 0.8. Both $\bar{C}_D$ and $\langle \overline{Nu} \rangle$ increase with increasing the amplitude ratio A^*. It is found that $\bar{C}_D$ increases by about 7.26% at $A^* = 0.4$ more than that at $A^* = 0$, Fig. 3*a* and Table 4. The surface- and time-averaged Nusselt number $\langle \overline{Nu} \rangle$ enhances about 2.24% at $A^* = 0.4$ more than that at $A^* = 0$, Fig. 3*b* and Table 4. Therefore, we chose the intermediate case of the pulsating flow where $f^* = 7$ and $A^* = 0.4$, to be compared with the results obtained from the steady case at $A^* = 0$. The time-mean drag coefficient $\bar{C}_D$ sharply increases with increasing A^* for $A^* > 0.3 – 0.8$, while $\langle \overline{Nu} \rangle$ increases with increasing A^* for $A^* > 0.3 – 0.6$, and then decreases to $A^* = 0.8$.

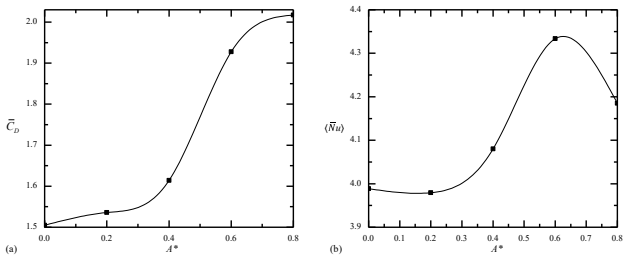

Fig. 3*. Effect on A^* (= 0.0 – 0.8) of (a) time-mean drag coefficient $\bar{C}_D$, and (b) surface- and time-averaged Nusselt number $\langle \overline{Nu} \rangle$, $f^* = 7$, and $Re = 100$.*

TABLE IV Comparison of the obtained results with the steady case and the pulsating flow at $r/R = 0$, $f^* = 7$, and variable amplitude ratio A^*.

A^*	$\langle \overline{Nu} \rangle$	(Increasing %)	$\bar{C}_D$	(Increasing %)
0.0	3.99	-	1.51	-
0.2	3.98	-0.2397	1.54	1.98
0.4	4.08	2.2844	1.61	6.62
0.6	4.3	8.6445	1.93	27.82
0.8	4.19	4.9234	2.017	33.57

The obtained results of $\bar{C}_D$ and $\langle \overline{Nu} \rangle$ at different amplitude ratios ($A^* = 0.2, 0.4, 0.6, 0.8$) and normalized frequency $f^* = 7$ are presented in Table 4. It is observed that $\bar{C}_D$ slightly increases by about 28% at $A^* = 0.6$ and reaches the maximum drag of about 34% at $A^* = 0.8$, as compared to that at the steady case ($A^* = 0$). The surface- and time-averaged Nusselt number $\langle \overline{Nu} \rangle$ is independent on the amplitude ratio upto $A^* = 0.2$, while largely increases with increasing A^* for $A^* = 0.2 – 0.6$. The maximum $\langle \overline{Nu} \rangle$ and maximum $\bar{C}_D$ are attributed to the maximum A^* at $f^* = 7$. At $A^* = 0.4$, $\langle \overline{Nu} \rangle$ increases about 2.28 % more than the steady case and corresponds to $\bar{C}_D$ (= 1.61) which increases about 7.26% more than the steady case without pulsating, Table 4 and Fig. 3.

The time-mean drag coefficient is sensitive to r/R and flow regimes as shown in Fig. 4a. The time-mean drag coefficient decreases with increasing r/R at $r/R \leq 0$ - 0.5. For the pulsating flow, $\bar{C}_D$ decreases from 1.6 to 1.44, while for the steady flow, $\bar{C}_D$ decreases from 1.51 to 1.37. For $r/R > 0.5$, $\bar{C}_D$ is independent on r/R. The time-mean drag coefficient for the pulsating flow is higher than that of the steady flow overall r/R. At $r/R = 0$ (square cylinder), $\bar{C}_D$ increases by about 7% for the pulsating flow, more than that of the steady flow. For the pulsating flow, $\bar{C}_D$ increases about 5.37% overall r/R, as shown in Fig. 4*a*. The surface- and time-averaged Nusselt number is affected by r/R as shown in (Fig. 4*b*). The surface- and time-averaged Nusselt number increases with increasing r/R for the pulsating flow from 4.1 to 5.1 and increases from 3.99 to 5.15 for the steady flow. The pulsating flow has a higher $\langle \overline{Nu} \rangle$ with a variation of about 2.26% more than that of the steady flow at $r/R = 0$. The steady flow has a higher $\langle \overline{Nu} \rangle$ about 0.55% more than the pulsating flow at $r/R = 0.75$.

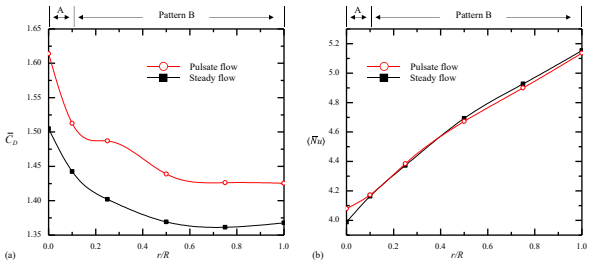

Fig. 4. *Effect of r/R on (a) time-mean drag coefficient $\bar{C}_D$, and (b) surface- and time-averaged Nusselt number $\langle \overline{Nu} \rangle$, $f^* = 7$, $Re = 100$, and $A^* = 0.4$.*

B. Flow structure:

Figure 5 shows the time mean streamlines of the flow around the cylinder surfaces at different frequencies f^* (= 0, 3.5, 7, 14, 21). The primary wake bubble length $L_p^* = (L_p/D)$, where L_p is defined as the distance from the cylinder center to the saddle point at zero velocity, as marked in Fig. 5. The primary wake bubble length decreases with increasing from 0 to 3.5, and independent on f^* at the range of $f^* = 3.5$ to 12, while sharply increases with increasing f^* from 12 to 21, as shown in Fig. 5*h*.

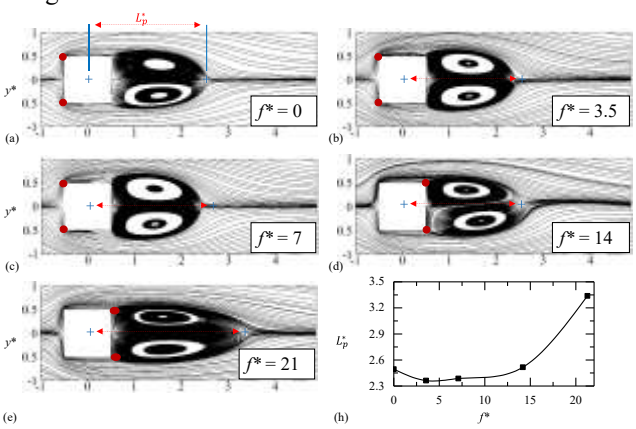

Fig. 5. *Time-mean streamlines of the pulsating flow ($A^* = 0.4$) around the cylinder at different frequencies (a - e) $f^* = 0$ - 21, and (f) Dependence of L_p^* on f^*, at $Re = 100$.*

From the relation between L_p^* and f^* in Fig. 5*h*. The primary wake bubble length sharply increases with increasing f^* from $f^* = 12$ to 21, as shown in Fig. 5*h*. The sharp decrease of $\bar{C}_D$ and $\langle \overline{Nu} \rangle$ is attributed to the increase of L_p^* that sharply increases with increasing the normalized frequency f^* from $f^* = 12$ to 21, as shown in Figs. 2 and 5*h*. The time-mean streamlines in Figs. 6 and 7 are introduced to present the effect of *r/R* on the flow structure around the cylinder surfaces for the pulsating flow ($A^* = 0.4$) and the steady flow case ($A^* = 0$), respectively, at $f^* = 7$. The variation of *r/R* has a significant effect on the wake bubble structure, wake bubble length L_p^*, the separation points, and its recirculation.

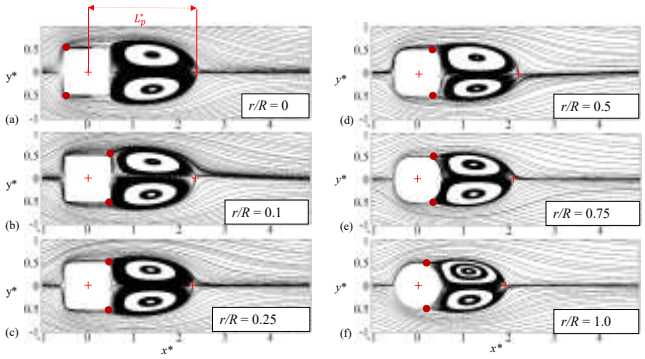

Fig. 6. Time-mean streamlines of the pulsating flow ($A^* = 0.4$) around the cylinder surfaces at different r/R (a - f) r/R = 0 - 1.0, respectively, at $f^* = 7$, and $Re = 100$.

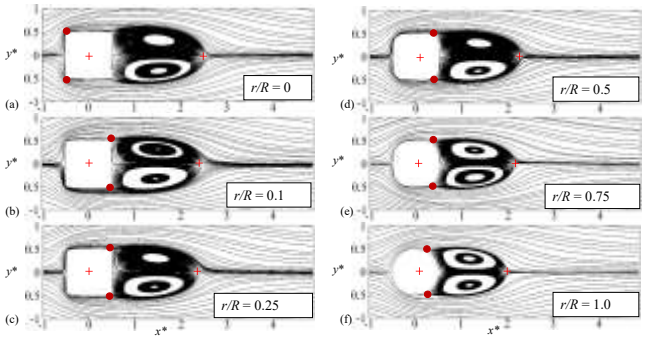

Fig. 7*. Time-mean streamlines of the steady flow ($A^* = 0$) around the cylinder surfaces at different r/R (a - f) r/R = 0 - 1.0, respectively, $f^* = 7$, and $Re = 100$.*

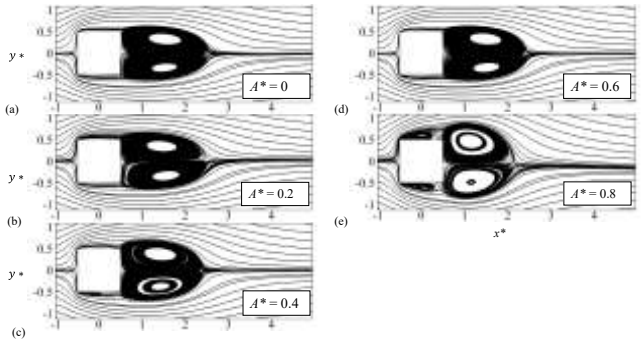

Fig. 8. *Time-mean streamlines of the pulsating flow around the cylinder for variable amplitude of A^* at $f^* = 7$, r/R = 0 (square cylinder), and $Re = 100$.*

From the introduced time mean streamlines of the steady case and pulsating flow at different *r/R*, we can classify the flow to the major flow patterns. The time-averaged streamlines for the pulsating flow of variable A^* (ranging from 0 to 0.8 with increments of 0.2) at $f^* = 7$ are presented in Figure 8. Figure 8 shows that for A^* values ranging from 0 to 0.7, the flow remains attached to the cylinder surfaces, while for A^* values ranging from 0.7 to 0.8, secondary bubbles form on the lateral sides of the cylinder. This can show the effect of the wake bubble length L_p^* on the amplitude ratio of the velocity oscillations A^*, at different A^* (= 0 – 0.8). Figure 9 presents the flow pattern map of the pulsating flow and the steady flow for different *r/R* = 0 – 1.0 at $f^* = 7$. Two major flow patterns

are observed with changing r/R, as shown in Figs. 6 - 9. Flow pattern (A) appears at small r/R, ($r/R \leq 0 - 0.1$). The flow separates from the two leading corners resulting in two secondary bubbles forming on the sides of the cylinder (Fig. 9*b*, *c*). The flow remains attached to the front sides of the cylinder (Region II). The size of the side bubbles over the cylinder surface for the pulsating flow is larger than that of the steady flow (Fig. 9*b*1, *c*1). Konstantinidis and Balabani, [25] investigated the wake structure of a circle cylinder in non-reversing flow by means of particle image velocimetry. They observed that the modification of the wake structure using the flow pulsation is caused by changes in the dynamics of vortex formation and shedding primarily in the near wake. Pattern (B) appears at large range of r/R, where $r/R > 0.1 - 1.0$ as shown in Fig. 9*a*. The separation of this pattern trailing-corners separation results in one primary wake bubble Region (III) as shown in Fig. 9*d*.

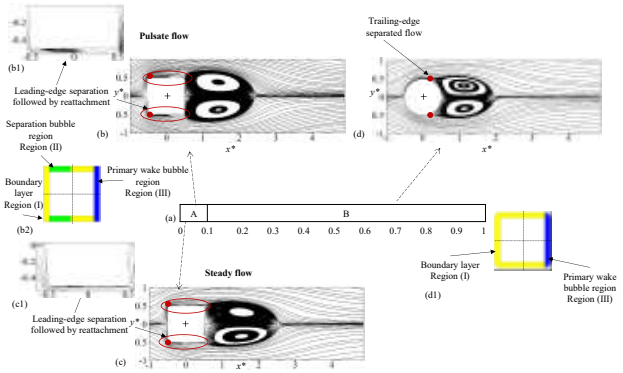

Fig. 9. *(a) Flow pattern map of the pulsating and steady flow at different r/R. Time-mean streamlines around the cylinder for (b) flow pattern A at r/R = 0 and A* = 0.4, (c) flow pattern A at r/R = 0 and A* = 0. Zoomed-in-view of the rear cylinder, (b1) pulsate flow (A* = 0.4), (c1) steady flow (A* = 0), (d) flow pattern B at r/R ≤ 0.1. Sketch of (b2) flow pattern A, (d1) flow pattern B, f* = 7, and Re = 100.*

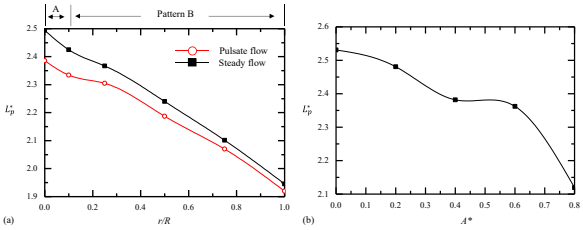

Fig. 10. *Effect of the wake bubble length L_p^* on (a) corner radius ratio r/R for the pulsating flow of A* = 0.4 and steady flow (A* = 0), (b) amplitude ratio of the velocity oscillations A*, for A* = 0 – 0.8, at f* = 7 and Re = 100.*

Figure 10 shows the effect of L_p^* on r/R for the pulsating flow case and steady flow case. The primary wake bubble length L_p^* decreases with increasing r/R as shown in Fig. 10. It is observed that L_p^* for the pulsating flow is less than that of the steady flow at any r/R, while $\bar{C}_D$ for the pulsating flow is larger than that of the steady flow, Figs. 4 and 10. This means that increasing A^* decreases L_p^* but increases the time-mean drag coefficient $\bar{C}_D$ at the same r/R, Figs. 4 and 10. The primary wake bubble length L_p^* decreases by about 19.45% for the pulsating flow and 22% for the steady case from $r/R = 0$ to $r/R = 1.0$, as shown in Fig. 10. Figure 10*b* shows the dependence of L_p^* on the amplitude ratio A^*. The primary wake bubble length gradually decreases with increasing A^* up to $A^* = 0.45$, after that L_p^* is independent of A^* (= 0.45 – 0.6), Fig. 10*b*. The primary wake bubble length decreases about 5.96% and 6.66% at $A^* = 0.4$ and $A^* = 0.6$, respectively, as compared to that of the steady case.

C. Cylinder-surface flow topology:

Figure 11 shows the effect of the time-averaged pressure coefficient $\bar{C}_p$, $\overline{Nu}$, and time-averaged skin friction coefficient $\bar{C}_f$ on the cylinder surfaces at different r/R, where $\bar{C}_f = \bar{\tau}_w / (0.5\rho U_\infty^2)$, $\bar{\tau}_w$ is the mean-wall shear stress. The time-averaged pressure coefficient decreases with increasing r/R at ($0° \leq \theta \leq 45°$) and ($315° \leq \theta \leq 360°$), Fig.11. The minimum $\bar{C}_p$ occurs at $\theta = 45°$ and 315°, for the steady flow, while the minimum $\bar{C}_p$ is shifted from 45° and 315° to 74° and 285°, respectively, for the pulsating flow. The time-averaged pressure coefficient decreases with increasing r/R at Region I, while increases with increasing r/R at the primary wake bubble region, Fig. 11*a*. The higher $\overline{Nu}$ is observed at Region I over the cylinder surfaces as shown in Fig. 11*b*. The time mean Nusselt number $\overline{Nu}$ enlarges with increasing r/R over the cylinder surfaces at Region I. For the steady flow, $\bar{C}_f$ and $\overline{Nu}$ peaks appear at $\theta = 45°$ and 315°, while for the pulsating flow $\bar{C}_f$ and $\overline{Nu}$ shift to 75° and 285°, respectively. Moreover, $\bar{C}_p$ is inversely linked to $\overline{Nu}$ at Region I. The time-averaged pressure coefficient corresponds to $\overline{Nu}$ as shown in Fig. 11*b*, *c*.

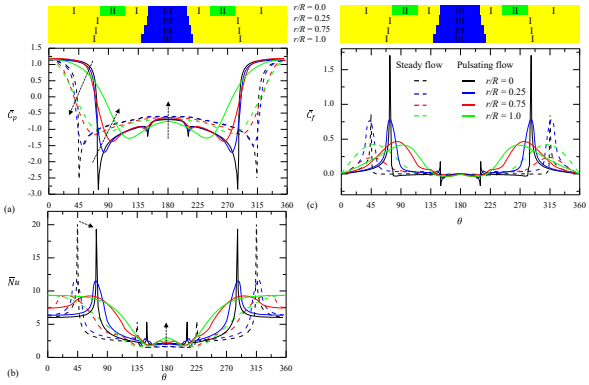

Fig. 11. *Dependence on θ of the pressure coefficient, Nusselt number, and skin friction coefficient for pulsating and steady flow at different r/R. (a) time-averaged pressure coefficient $\bar{C}_p$, (b) time- averaged Nusselt number $\overline{Nu}$, and (c) time-averaged skin friction coefficient $\bar{C}_f$ around the cylinder, A* = 0.4, f* = 7, and Re = 100.*

D. Wake Structure:

The flow structure, heat transfer, and fluctuation forces over the cylinder are all affected by the flow separation, wake recirculation bubble, vortex shedding, and vortex formation length. The contours of normalized instantaneous vorticity w_z^* ($= w_z \times D/U_\infty$) for pulsating and steady flow are introduced in Figs. 12 and 13, respectively. The flow structure is unsteady

and characterized by vortices that appear at all flow regimes and for all *r/R*. The upper core (negative) and lower core (positive) instantaneous vorticity w_z^* are marked to emphasize the vortex intensity and dissipation at each *r/R*. The upper core and lower core of the normalized instantaneous vorticity w_z^* are presented for the pulsating flow and the steady flow as shown in Figs. 12 and 13. This shows that w_z^* is slightly affected by the pulsating flow ($A^* = 0.4$) more than that of the steady flow ($A^* = 0$), Figs. 12 and 13. Figure 14 shows the isocontours of the normalized instantaneous vorticity w_z^* at *r/R* = 0, for the steady case and the pulsating flow at acceleration and deceleration. The obtained vortex shedding at deceleration has an effect on the size of the bubbles that are formed on the sides of the cylinder. These side bubbles increase for the pulsating flow at $A^* = 0.4$, more than those of the steady flow at $A^* = 0$ and $f^* = 7$.

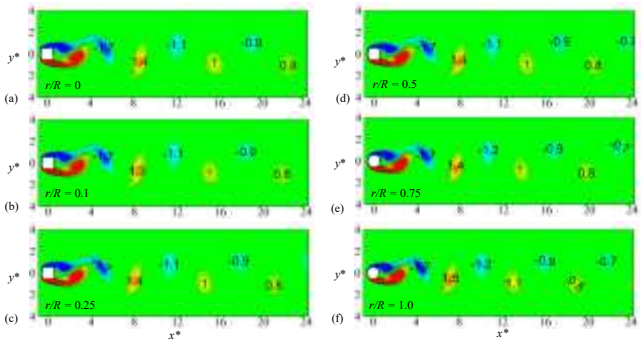

Fig. 12. *Iso-contours of the normalized instantaneous vorticity* $\omega_z^* = \omega_z \times \frac{D}{U_\infty}$, *for different r/R (= 0 - 1.0) of the pulsating flow at A* = 0.4, f* = 7, and Re = 100.*

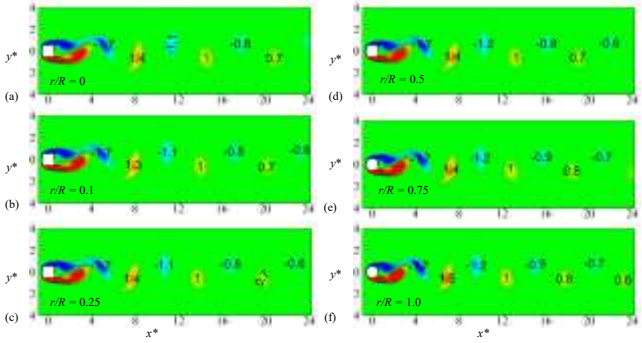

Fig. 13. *Iso-contours of the normalized instantaneous vorticity* $\omega_z^* = \omega_z \times D/U_\infty$, *for the steady flow (A* = 0), at different r/R (= 0 - 1.0), f* = 7, and Re = 100.*

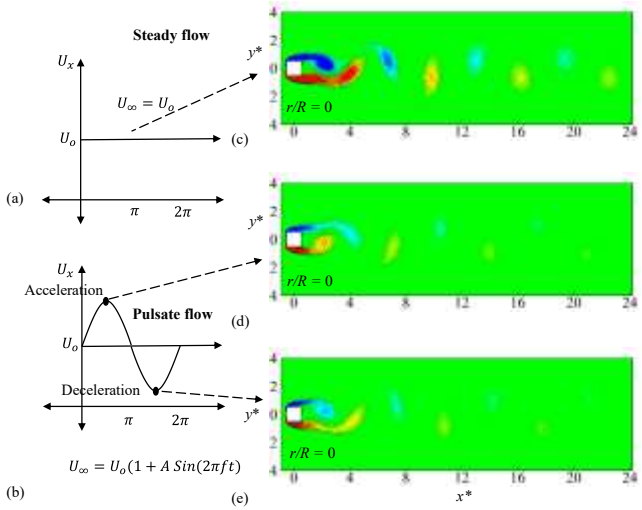

Fig. 14. *Isocontours of the normalized instantaneous vorticity* $\omega_z^* = \omega_z \times \frac{D}{U_\infty}$, *at r/R = 0, for (a, c) steady flow (A* = 0), (b) pulsating flow (A* = 0.4) at (d) acceleration, and (e) deceleration, for f* = 7, and Re = 100.*

IV. CONCLUSION

A numerical study is conducted to investigate the flow structure and heat transfer over an isothermal cylinder with varying geometries of *r/R* at *Re* = 100. The study focuses on examining the effects of flow topology, heat transfer, and global forces on *r/R*, which varies from 0 to 1, for both pulsating flow (at $A^* = 0.4$ and $f^* = 7$) and steady flow (at $A^* = 0$). Numerical comparisons are conducted between the obtained results of the $\bar{C}_D$ and $\langle \overline{Nu} \rangle$ with those obtained from the literature for both steady flow ($A^* = 0$) and pulsating flow ($A^* = 0.4$) at $f^* = 7$, and *r/R* = 0. The effect of $\bar{C}_D$ and $\langle \overline{Nu} \rangle$ on the normalized frequency is investigated for different frequency $f^* = 0$, 3.5, 7, 14, and 21. Additionally, the dependence of the $\bar{C}_D$ and $\langle \overline{Nu} \rangle$ on the amplitude ratio A^*, where $A^* = 0$, 0.2, 0.4, 0.6 and 0.8. Subsequently, appropriate values of $A^* = 0.4$ and $f^* = 7$ are chosen for investigating the effect of flow structure and heat transfer on *r/R* at *Re* = 100. The main findings can be summarized as follows:

- It is observed that $\bar{C}_D$ decreases with increasing *r/R*.
- The time-averaged drag coefficient for the pulsating flow is higher than that of the steady flow overall *r/R*.
- At *r/R* = 0 (square cylinder), $\bar{C}_D$ increases by about 7% for the pulsating flow, more than that of the steady flow.
- The surface- and time-averaged Nusselt number $\langle \overline{Nu} \rangle$ increases with increasing *r/R* for both flow patterns.

- The pulsating flow enhances $\langle \overline{Nu} \rangle$ at small *r/R* (= 0 – 0.1), for frequency f^* (= 7) and amplitude ratio $A^* = 0.4$.
- Two major flow patterns appear around the cylinder surfaces with changing *r/R*.
- Flow pattern A appears at *r/R* < 0.1, where leading-corners separation and two secondary bubbles appeared on the side surfaces of the cylinder.
- Flow pattern B appears at *r/R* from 0.1 to 1.0, where trailing-corners separation occurs.
- The flow regime of both pulsating and steady flows is characterized by unsteadiness and alternating Kármán vortices for different *r/R* values.

As a future endeavor, we can investigate the flow topology and heat transfer for different frequencies and amplitudes, while varying the corner radius ratio and angle of attack.

ACKNOWLEDGMENT

This work was partially supported by the Science and Technology Development Fund (STDF) of Egypt, project No: 39385.

REFERENCES

[1] B. Kumar, G. P. Srivastava, M. Kumar, and A. K. Patil, "A review of heat transfer and fluid flow mechanism in heat exchanger tube with inserts," *Chemical Engineering and Processing: Process Intensification*, vol. 123, pp. 126–137, 2018, doi: 10.1016/j.cep.2017.11.007.

[2] S. Miran and C. H. Sohn, "Influence of incidence angle on the aerodynamic characteristics of square cylinders with rounded corners," *International Journal of Numerical Methods for Heat & Fluid Flow*, vol. 26, no. 1, pp. 269–283, Jan. 2016, doi: 10.1108/HFF-02-2015-0058.

[3] Z. Xu, Z. Han, J. Wang, and Z. Liu, "The characteristics of heat transfer and flow resistance in a rectangular channel with vortex generators," *International Journal of Heat and Mass Transfer*, vol. 116, pp. 61–72, 2018, doi: 10.1016/j.ijheatmasstransfer.2017.08.083.

[4] A. K. Saha, G. Biswas, and K. Muralidhar, "Three-dimensional study of flow past a square cylinder at low Reynolds numbers," *International Journal of Heat and Fluid Flow*, vol. 24, no. 1, pp. 54–66, 2003, doi: 10.1016/S0142-727X(02)00208-4.

[5] T. Abdelhamid, A. G. Rahma, and R. Chen, "Flow structure around a curved corner cylinder with varied attack angles," in *2021 International Conference on Electronic Engineering (ICEEM)*, 2021, pp. 1–4, doi: 10.1109/ICEEM52022.2021.9480633.

[6] F. Zafar and M. M. Alam, "Flow structure around and heat transfer from cylinders modified from square to circular," *Physics of Fluids*, vol. 31, no. 8, 2019, doi: 10.1063/1.5109693.

[7] C. Gau, J. M. Wu, and C. Y. Liang, "Heat transfer enhancement and vortex flow structure over a heated cylinder oscillating in the crossflow direction," *Journal of Heat Transfer*, vol. 121, no. 4, pp. 789–795, 1999, doi: 10.1115/1.2826067.

[8] H. M. Badr, "Effect of free-stream fluctuations on laminar forced convection from a straight tube," *International Journal of Heat and Mass Transfer*, vol. 40, no. 15, pp. 3653–3662, 1997, doi: 10.1016/S0017-9310(96)00387-0.

[9] S. K. Singh and M. Engg, "Influence of rounding corners on unsteady flow and heat transfer around a square cylinder," no. 5, pp. 6–12, 2015.

[10] T. Ambreen and M. H. Kim, "Flow and heat transfer characteristics over a square cylinder with corner modifications," *International Journal of Heat and Mass Transfer*, vol. 117, pp. 50–57, 2018, doi: 10.1016/j.ijheatmasstransfer.2017.09.132.

[11] M. Eslami, A. Hozhabr, and F. Lotfipour, "Asymmetric Distribution of Longitudinal Fins Around a Tube in Cross Flow: Optimization with CFD Modeling," *Iranian Journal of Science and Technology, Transactions of Mechanical Engineering*, vol. 47, no. 2, pp. 497–511, 2023, doi: 10.1007/s40997-022-00549-2.

[12] M. Yadegari, A. Bak Khoshnevis, and M. Boloki, "An Experimental Investigation of the Effects of Helical Strakes on the Characteristics of the Wake around the Circular Cylinder," *Iranian Journal of Science and Technology, Transactions of Mechanical Engineering*, vol. 47, no. 1, pp. 67–80, 2023, doi: 10.1007/s40997-022-00494-0.

[13] M. Ansari, S. T. O. Naeeni, and M. Moradi, "Investigating the Flow and Heat Transfer Characteristics of Two Co/Counter-Rotating Circular Cylinders at a Low Reynolds Number," *Iranian Journal of Science and Technology, Transactions of Mechanical Engineering*, 2023, doi: 10.1007/s40997-023-00657-7.

[14] O. A. Gaheen, E. Benini, M. A. Khalifa, M. E. El-Salamony, and M. A. Aziz, "Experimental investigation on the convection heat transfer enhancement for heated cylinder using pulsated flow," *Thermal Science and Engineering Progress*, vol. 26, no. August, p. 101055, 2021, doi: 10.1016/j.tsep.2021.101055.

[15] T. Abdelhamid, A. G. Rahma, M. Alam, and R. Chen, "Heat transfer and flow around curved corner cylinder : effect of attack angle," *SN Applied Sciences*, 2023, doi: 10.1007/s42452-023-05377-w.

[16] S. Gupta, S. A. Patel, and R. P. Chhabra, "Pulsatile flow of power-law fluids over a heated cylinder: Flow and heat transfer characteristics," *International Journal of Thermal Sciences*, vol. 152, no. January, p. 106330, 2020, doi:

10.1016/j.ijthermalsci.2020.106330.

[17] M. Khalid, R. Haseeb, and S. F. Anwer, "Numerical simulation of pulsatile flow past heated square cylinders," *Lecture Notes in Mechanical Engineering*, pp. 449–456, 2017, doi: 10.1007/978-81-322-2743-4_43.

[18] J. Y. Yu, W. Lin, and X. T. Zheng, "Effect on the flow and heat transfer characteristics for sinusoidal pulsating laminar flow in a heated square cylinder," *Heat and Mass Transfer/Waerme- und Stoffuebertragung*, vol. 50, no. 6, pp. 849–864, 2014, doi: 10.1007/s00231-014-1294-4.

[19] A. Saxena and E. Y. K. Ng, "Steady and pulsating flow past a heated rectangular cylinder(s) in a channel," *Journal of Thermophysics and Heat Transfer*, vol. 32, no. 2, pp. 401–413, 2018, doi: 10.2514/1.T5265.

[20] T. Abdelhamid, M. M. Alam, and M. Islam, "Heat transfer and flow around cylinder: Effect of corner radius and Reynolds number," *International Journal of Heat and Mass Transfer*, vol. 171, p. 121105, 2021, doi: 10.1016/j.ijheatmasstransfer.2021.121105.

[21] A. Sohankar, C. Norberg, and L. Davidson, "Low-Reynolds-number flow around a square cylinder at incidence: Study of blockage, onset of vortex shedding and outlet boundary condition," *International Journal for Numerical Methods in Fluids*, vol. 26, no. 1, pp. 39–56, 1998, doi: 10.1002/(sici)1097-0363(19980115)26:1<39::aid-fld623>3.0.co;2-p.

[22] Q. Zheng and M. M. Alam, "Intrinsic features of flow past three square prisms in side-by-side arrangement," *Journal of Fluid Mechanics*, vol. 826, no. October, pp. 996–1003, 2017, doi: 10.1017/jfm.2017.378.

[23] M. M. Alam, T. Abdelhamid, and A. Sohankar, "Effect of cylinder corner radius and attack angle on heat transfer and flow topology," *International Journal of Mechanical Sciences*, vol. 175, no. January, p. 105566, 2020, doi: 10.1016/j.ijmecsci.2020.105566.

[24] A. Sharma and V. Eswaran, "Heat and fluid flow across a square cylinder in the two-dimensional laminar flow regime," *Numerical Heat Transfer; Part A: Applications*, vol. 45, no. 3, pp. 247–269, 2004, doi: 10.1080/10407780490278562.